Mass transport in catalytic pores of GDE-based CO_2 electroreduction systems

Divya Bohra,[†] Jehanzeb H. Chaudhry,[‡] Thomas Burdyny,[†] Evgeny A. Pidko,[¶] and Wilson A. Smith[*,†,§,‖]

[†]*Materials for Energy Conversion and Storage (MECS), Department of Chemical Engineering, Delft University of Technology, Delft, The Netherlands*

[‡]*Department of Mathematics and Statistics, University of New Mexico, Albuquerque, USA*

[¶]*Inorganic Systems Engineering (ISE), Department of Chemical Engineering, Delft University of Technology, Delft, The Netherlands*

[§]*Department of Chemical and Biological Engineering, University of Colorado Boulder, Boulder, USA*

[‖]*National Renewable Energy Lab, Golden, USA*

E-mail: wilson.smith@colorado.edu

Abstract

Gas diffusion electrode (GDE)-based setups have shown promising performance for CO_2 electrocatalysis and further development of these systems will be important on the path to industrial feasibility. In this article, we model an effective catalyst pore within a GDE-based flow-cell to study the influence of the catalyst structure and operating conditions on the reaction environment for CO_2 electrocatalysis at practically relevant current densities. Using a generalized modified Poisson-Nernst-Planck (GMPNP) 3D model of the nanoporous catalyst layer, we show that the length of the catalyst pore as well as the boundary conditions at the gas-electrolyte and electrolyte-electrolyte interfaces across this length are highly influential parameters for determining the conditions

within the catalyst pore. Pores with the same catalytic surface area can have very different reaction environments depending primarily on the pore length and not the pore radius. Properties such as electrolyte pH and buffer breakdown, ionic strength and CO_2 concentration are also highly-sensitive to the catalyst layer thickness, gas pressure, electrolyte flow rate and the flow-channel geometry. The applied potential impacts the concentration of ionic species in the pore, which in turn determines the solubility of CO_2 available for the reaction. Our results underline the need to understand and manage transport within GDE-based electrocatalysis systems as an essential means to control catalyst performance. Benchmarking of GDE-based electrocatalytic systems against their structural and operational parameters will be important for achieving improvements in performance that can be ultimately translated to large-scale operation.

Introduction

The solubility of carbon dioxide (CO_2) in aqueous electrolytes under ambient conditions is $\sim$ 33 mM. In a system design where the electrolyte is saturated with dissolved CO_2, mass transport limits the achievable CO_2 reduction current density to below 50 mA/cm^2 irrespective of the nature of the catalyst employed.[1–11] For the process to be economically feasible, current densities in the order of $\sim$ 200 mA/cm^2 and greater are estimated to be required in addition to the selectivity, over-potential and stability targets.[12–14] Gas diffusion electrodes (GDE) based cell designs have been demonstrated to successfully overcome this mass transfer limitation in CO_2 electrochemical reduction (eCO_2R) systems.[15–21]

The classical GDE-based eCO_2R systems studied in literature are flow-cells or microfluidic cells following a general setup as shown in Figure 1a for the cathode half of the reactor.[22–31] The GDE cathode itself is typically composed of 3 layers: 1) the gas diffusion layer (GDL) which acts as a gas distribution network for the incoming CO_2 and outgoing gaseous products to and from the catalyst, 2) a thin micro-porous layer (MPL) of carbon nanoparticles deposited on the GDL which acts as the current collector and 3) the electrocatalyst layer

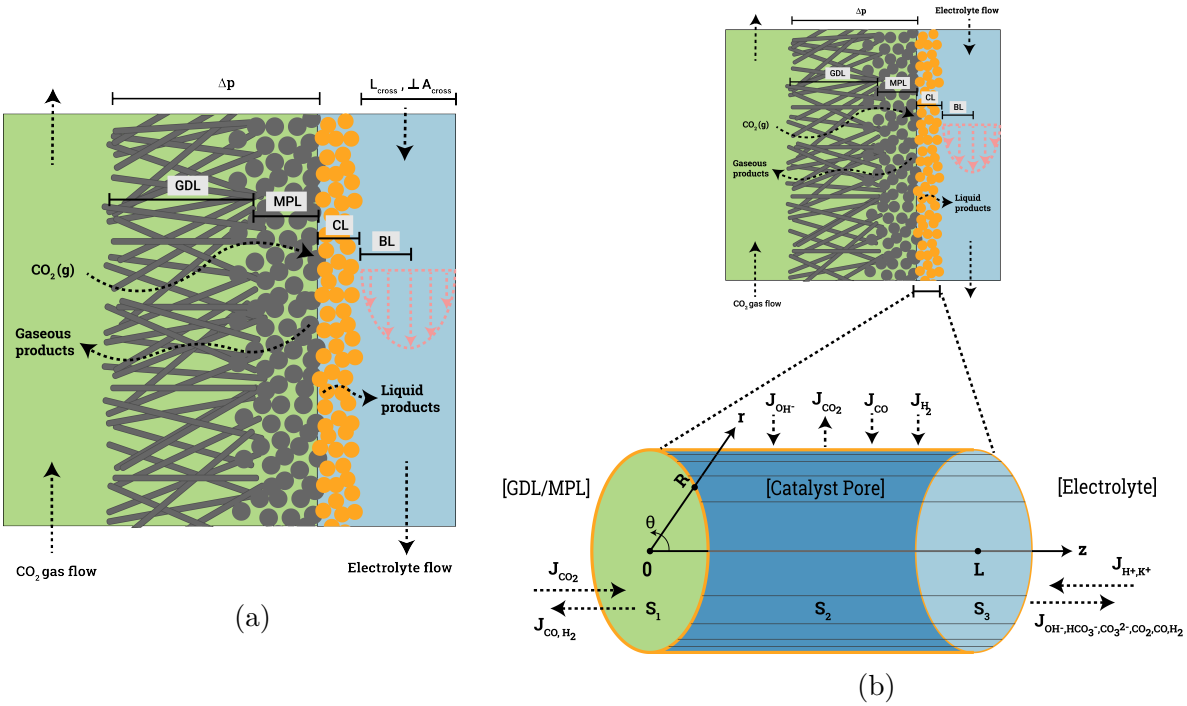

Figure 1: (a) Illustration of a typical cathode setup in a GDE-based flow-cell for CO_2 reduction. The green and the blue zones signify the gas and the aqueous phase, respectively. The dotted arrows represent the general direction of the flow. GDL: gas diffusion layer, MPL: micro-porous layer, CL: catalyst layer, BL: boundary layer, L_{cross}: cross-sectional width of the liquid flow channel, A_{cross}: perpendicular cross-sectional area of the liquid flow channel. (b) Zoomed-in illustration of the effective cylindrical pore used as the model system. S_1, S_2 and S_3 are the simulation domain boundary surfaces and represent the gas-electrolyte interface at the pore entry, the cylindrical catalyst surface and the electrolyte-electrolyte interface at the pore exit, respectively. R is the pore radius and L is the pore length. r, z and Θ represent the radial, longitudinal and azimuthal axes, respectively. $\mathbf{J}_i$ stands for the flux of species i normal to the respective surface.

(CL) which is deposited on top of the MPL.

During operation of a GDE, a gas stream of pure CO_2 flows from the inlet of a channel along the GDL, leaving the gas channel with the gaseous products of the catalysis. Similarly, a liquid flow channel facing the catalyst of the GDE continuously circulates the aqueous electrolyte. The diffusion length of CO_2 to the catalyst surface in such a setup is several orders of magnitude smaller than in a system where the CO_2 dissolved in the bulk electrolyte has to diffuse to the cathode surface (from here-on referred to as an H-cell type setup), resulting in a drastic improvement in the achievable current density attributed to eCO_2R. There are

practical advantages to electrolyte-flow systems that make them a desirable setup for studying and optimizing eCO_2R such as: a higher control of reaction conditions and therefore catalyst selectivity and activity through the composition of the electrolyte,[17,22,25,27,28] better water management for the catalysis and for membrane stability, and ease of liquid product sampling due to continuous flow.[24,29]

Other system configurations such as membrane-electrode assemblies (MEA) inspired by fuel cell architectures have been proposed in literature as an alternative to flow-cells.[24,32–39] MEAs reduce the impacts of flooding due to the elimination of liquid electrolyte flow, and can potentially achieve even higher eCO_2R current densities due to better access to CO_2 from the gas phase. These advantages make MEA setups an attractive candidate for systems operating at practically relevant scales. However, controlling product selectivity, water management, salt precipitation-related fouling as well as membrane stability can be a challenge in these setups.[32,40–42] There is considerable variation in the cell-design and performance analysis among the initial MEA studies, making a comparison between the different approaches difficult. Further systematic studies are required to establish best design and operational practices for optimal performance for the respective eCO_2R products.

In this report, we will focus on modeling the mass transport within the CL in flow-cell type systems as depicted in Figure 1a. As the number of experimental studies using GDE-based flow-cells increase, there is a rising need to compliment these with simulations to better understand the effect of the various system parameters on the measured performance. The porous nature of the catalyst layer in the flow-cell systems are much more complex than the H-cell setups that have been modeled extensively in literature so far,[43–45] making it difficult to isolate and experimentally measure the effects of the various parameters. At substantial current densities, the structure, porosity, exposed surface area and width of a deposited catalyst layer will impact the environment of a CL pore network, necessitating the consideration of catalyst structure when interpreting experimental electrochemical performance. Additionally, flow-cells present several design and operational handles to influence reaction

conditions within the CL.

Electrolyte composition and pH within the catalyst layer of the GDE is understood to be an influential parameter for the selectivity of CO_2 reduction.[21] Multiple experimental studies using flow-cells observe a correlation between the electrolyte and C-C coupling reaction on Cu catalysts to form ethylene,[22,27,28] CO Faradaic efficiency on Ag[24–26,31] and formate production on Sn.[29] An optimal control of the reaction environment is expected to have a dramatic influence on the catalyst performance as has also been observed in studies in H-cell setups.[46–52] Previously reported models pertaining to GDE flow-cell configurations assume a one-dimensional (1D) structure-less approach to simulating transport within the flow-cell CL.[27,53–55] Here we simulate the reaction environment within an effective three-dimensional (3D) catalytic pore of a GDE-based flow-cell to understand the influence of changing pore structure and boundary conditions on the electrolyte composition during steady-state operation at practically relevant current densities ($> 50\ \mathrm{mA/cm^2}$, see Figure 2b). We use the generalized modified Poisson-Nernst-Planck (GMPNP) model[56,57] as reported recently by us for a 1D H-cell setup case,[43] and extend it for 3D cylindrical pores with appropriate boundary conditions relevant for laboratory flow-cell setups.

Our analysis of the GDE flow-cell finds that the length is one of the most influential structural parameters of the catalyst layer for the median pH and ion concentration within the pore. The length of the pore becomes an important parameter due to the fact that the fluxes of species at the gas-electrolyte and electrolyte-electrolyte interface are large enough to compete with the rates of the reactive and diffusive processes within the pore. As a result, the boundary conditions for the catalyst layer such as the gas pressure and the electrolyte flow rate play a very important role in determining optimal reaction conditions for the catalyst. By comparing the performance of the GMPNP model with a reaction-diffusion model, we discuss the relevance of the applied potential for ionic concentration, CO_2 solubility and edge effects within the pore. GDE-based flow-cells are characterized by a narrow and porous catalyst layer surrounded by interfaces that have a major influence on transport of species

in and out of the reactive domain. The reaction environment in GDE setups is expected to deviate significantly from what is encountered in eCO_2R in H-cell setups and therefore a considerably different performance with respect to onset-potential, selectivity and activity can be expected.

Model description

Figure 1b illustrates the cylindrical pore domain used for the GMPNP simulation. This is an idealization of the CL for the purposes of deduction. The pore structures in the actual CL deposited on the GDL are expected to be highly heterogeneous as reported in a very recent tomography study on Ag GDE cathode.[58] We assume the catalytic pore to be completely flooded with electrolyte such that the gas-electrolyte interface is located at the pore entry (the boundary between the MPL and CL, S_1). We believe that this is a reasonable assumption for a metal catalyst pore with small radii at a reducing potential and that a vast majority of current density in flow-cell systems can be attributed to the double-phase electrolyte-catalyst boundary (S_2) like in case of an H-cell. We use CO producing catalysts as a test case for our simulations due to the prevalence of several experimental studies using GDEs showing promising results for CO_2 reduction to CO.[59–62] The following sections discuss the boundary conditions assumed at S_1, S_2 and S_3 in detail. The values of the constants used in the model can be found in the Parameters section in the SI. Parameters depicted in bold lettering imply vectors.

Gas-electrolyte interface (S_1)

The surface S_1 represents the gas-electrolyte interface located at the boundary between the MPL and the catalyst layer. The gas phase is assumed to be composed of 95% CO_2, 4.5% carbon monoxide (CO) and 0.5% hydrogen (H_2) and the pressure at S_1, p_1 is assumed to be 1 bar. We have ignored the presence of humidity in the gas stream and evaporation of the

electrolyte. The gas phase composition for CO producing GDE setups have not been reported for experimental setups in literature. For this reason we assume the gas phase to consist of a high % of CO_2 based on the fact that single-pass conversion efficiency for eCO_2R is typically low for lab-scale flow-cells. In practice, several factors such as the incoming gas-phase CO_2 flow rate, the Faradaic efficiency of CO_2 reduction, the current density and the transport characteristics of the GDL and rate of the flux of the product gases across the gas-electrolyte interface will determine the steady-state composition at S_1. For the model, the interface S_1 is considered to be in equilibrium and Dirichlet boundary conditions are assumed for CO_2, CO and H_2 concentrations at S_1 as per the equation (1). The assumption of equilibrium at the gas-liquid interface is valid in the majority of situations, except when very high mass transfer rates are present at the interface.[63] This can possibly be the case for the flux of the product species CO and H_2 across S_1 which are present in low concentrations in the gas phase and have relatively low solubility in the electrolyte. This is not seen as an issue for resolving the reaction environment within the pore, since, in addition to their low solubility, CO and H_2 do not interact with the electric field nor participate in the homogeneous reaction kinetics. Such factors require further attention for multi-carbon product formation where aqueous CO concentrations are expected to be important.

$$C_i^{S1} = H_i p_1 y_i \rho_e \tag{1}$$

where H_i is Henry's constant for species i (in mol·kg^{-1}·bar^{-1}), p_1 is the gas phase pressure at S_1 (in bar), y_i is the mole fraction of i at S_1, ρ_e is the density of the electrolyte (assumed as water density, not adjusted for ion concentration for simplicity, in kg·m^{-3} at 25°C) and C_i^{S1} is the concentration of species i at S_1 (in mM). H_{CO_2} is calculated using Sechenov equation[64,65] (see section Model details in the SI) to account for the effect of ion concentrations in the pore. Median values of ion concentrations in the pore are used at every time step to iteratively adjust the value of H_{CO_2} to determine the Dirichlet condition at S_1. The fluxes ($\mathbf{J}_i$) of all

species except CO_2, CO and H_2 are considered to be 0 at S_1 (no-flux boundary condition). Dirichlet boundary condition is used for the potential at S_1 as given in equation (3).

$$\mathbf{J}_{HCO_3^-,CO_3^{2-},K^+,H^+,OH^-}|_{z=0,x,y,t} = 0 \tag{2}$$

$$\phi|_{z=0,x,y,t} = 0 \tag{3}$$

Catalyst surface (S_2)

The following heterogeneous reactions are considered to be occurring at the cathode surface S_2 during eCO_2R. We assume CO producing catalysts such as Ag/Au as our test case.

$$CO_2(aq) + H_2O + 2\,e^- \rightleftharpoons CO(g) + 2\,OH^- \tag{4}$$

$$2\,H_2O + 2\,e^- \rightleftharpoons H_2(g) + 2\,OH^- \tag{5}$$

A total current density (I_{total}) and Faradaic efficiency (FE) distribution (ratio of electrons consumed for H_2 production vs CO) is assumed for the simulations. I_{total} is assumed to be either normalised by the electrochemically active surface area (I_{ECSA}) or the geometrical surface area (I_{geom}) which will be defined later in this section. No direct consumption of H^+ is assumed since the associated current will be negligible especially at the high current densities associated with flow-cells. The flux of the solution species at the surface is given by the equations (6) - (10). r=R in our simulations is assumed to be the outer Helmholtz plane (OHP) since there is no charge density in the Stern layer by definition. The factor of 0.5 in the equations (7) - (9) comes from the product to electron stoichiometry of the reactions (4)

- (5). We assume no bubble formation of the product species within the catalyst pore and therefore also no convection or turbulence effects within the pore due to bubbling.

$$\mathbf{J}_{HCO_3^-,CO_3^{2-},K^+}|_{\sqrt{x^2+y^2}=R,z,t} = 0 \tag{6}$$

$$\mathbf{J}_{CO_2}|_{\sqrt{x^2+y^2}=R,z,t} = 0.5 \times \frac{I_{total}}{F} \times FE_{CO} \tag{7}$$

$$\mathbf{J}_{CO}|_{\sqrt{x^2+y^2}=R,z,t} = -0.5 \times \frac{I_{total}}{F} \times FE_{CO} \tag{8}$$

$$\mathbf{J}_{H_2}|_{\sqrt{x^2+y^2}=R,z,t} = -0.5 \times \frac{I_{total}}{F} \times FE_{H_2} \tag{9}$$

$$\mathbf{J}_{OH^-}|_{\sqrt{x^2+y^2}=R,z,t} = -\frac{I_{total}}{F} \tag{10}$$

where F is the Faraday's constant and FE_{CO} and FE_{H_2} are assumed to be 95% and 5%, respectively. Dirichlet boundary condition is used for the potential at S_2 as given in equation (11) where V_{app} is the applied voltage in V.

$$\phi|_{\sqrt{x^2+y^2}=R,z,t} = V_{app} \tag{11}$$

Electrolyte-electrolyte interface (S_3)

We assume an electrolyte concentration of 1 M $KHCO_3$ as the bulk solution with the electrolyte flow parallel to the catalyst surface with a flow velocity $\mathbf{v}_e$ in $m^3 \cdot s^{-1}$. The flux of species i across the surface S_3 is assumed to depend linearly on the concentration gradient between S_3 and the bulk electrolyte solution as per the equation (12). We have assumed a very small concentration (1 % of equilibrium concentration at S_1) of CO and H_2 in the bulk

solution to be able to normalize the concentrations of both species to solve the GMPNP equations and to define the driving force for the flux in equation (12). Physically, this assumption implies that although, a majority of the CO and H_2 produced leave the system through the gas-liquid interface at S_1, a small quantity also moves into the bulk electrolyte through the liquid-liquid interface S_3 due to diffusive and convective fluxes. The value of 1% is arbitrarily chosen for the current simulations. Experimental data or models with more detailed treatment of CO and H_2 mass transport through the system can be used to better inform the concentration of CO and H_2 into the bulk electrolyte flow at steady state as a function of the operating conditions.

$$\mathbf{J}_i^e|_{z=L,x,y,t} = k_i^e(C_i^{S_3} - C_i^0) \quad i = \mathrm{CO_2}, \mathrm{CO}, \mathrm{H_2}, \mathrm{HCO_3^-}, \mathrm{CO_3^{2-}}, \mathrm{H^+}, \mathrm{OH^-}, \mathrm{K^+} \tag{12}$$

$$Sh = \frac{k_i^e}{D_i/L_c} = 1.017(\frac{2L_c}{L_{cross}}ReSc)^{1/3} \tag{13}$$

$$Re = \frac{\rho_e|\mathbf{v}_e|L_c}{\mu_e A_{cross}} \tag{14}$$

$$Sc = \frac{\mu_e}{\rho_e D_i} \tag{15}$$

where k_i^e is the convective mass transfer coefficient in $\mathrm{m{\cdot}s^{-1}}$ derived using the Sherwood number (Sh) as per equation (13).[63] $C_i^{S_3}$ and C_i^0 are the concentrations of species i at S_3 and in the bulk electrolyte, respectively (in mM). Equation (13) is applicable for laminar flow over a flat plate of length L_c (in m), which in this case, is the length of the catalyst along which the electrolyte is flowing, for an electrolyte film thickness assumed to be half of the cross-sectional width of the liquid channel ($L_{cross}/2$, in m) and a flow cross-section of A_{cross} (in $\mathrm{m^2}$). Re and Sc are Reynolds and Schmidt numbers respectively and are given by equations (14) and (15). ρ_e and μ_e are density (in $\mathrm{kg{\cdot}m^{-3}}$ at 25°C) and viscosity (in

$kg{\cdot}m^{-1}{\cdot}s^{-1}$ at 1 atm, 25°C) of the electrolyte, respectively and are assumed be that of pure water. Dirichlet boundary condition is used for the potential at S_3 as given in equation (16).

$$\phi|_{z=L,x,y,t} = 0 \tag{16}$$

GMPNP system of equations

The generalized modified Poisson-Nernst-Planck (GMPNP) equations used to model the mass transport of species in the electrolyte within the cylindrical pore are analogous to the equations used in reference 43.

$$\frac{\partial C_i}{\partial t} = -\nabla \cdot \mathbf{J}_i + \sum_j R_i \tag{17}$$

where C_i is the concentration of species i, t is time, j is the index of the homogeneous reaction in solution, R_i is the rate of production of species i due to the homogeneous reaction j as given by equations (9) to (13) in the SI and $\mathbf{J}_i$ is the flux of species i given by:

$$\mathbf{J}_i = -D_i^{eff}\nabla C_i - \frac{D_i^{eff} C_i z_i F}{R_G T}\nabla\phi - D_i^{eff} C_i \left(\frac{N_A \sum_{i=1}^{n} a_i^3 \nabla C_i}{1 - N_A \sum_{i=1}^{n} a_i^3 C_i}\right) \tag{18}$$

$$D_i^{eff} = \frac{D_i \epsilon \delta}{\tau^2} \tag{19}$$

where D_i^{eff} is the effective diffusion coefficient of species i given by equation (19),[66] z_i is the charge of species i, R_G is the gas constant, T is the temperature, N_A is the Avogadro's constant and a_i is the effective solvated diameter of the species i. In equation (19), D_i is the diffusion coefficient, ϵ, δ and τ are the effective porosity, constrictivity and tortuosity of the catalyst layer, respectively (assumed to be 0.5, 1.5 and 0.9, respectively). Equation (17) needs to be solved self-consistently with the Poisson equation given by:

$$\nabla \cdot (\varepsilon_0 \varepsilon_r \nabla \phi) = -F \sum_{i=1}^{n} z_i C_i \tag{20}$$

where ε_0 is the permittivity of vacuum, ε_r is the relative permittivity of the electrolyte and ϕ is the potential. The relative permittivity in equation (20) is assumed to vary with cation concentration as given by equation (21).[67,68] The concentration terms in the equation (21) are in M. M_{water} is the molarity of water at room temperature taken to be 55 M and the parameters w_i are the total number of water molecules held by the cation i. ε_r^0 is taken to be 80.1 equal to the relative permittivity of water at room temperature whereas ε_r^{min} is the dielectric constant of water under the condition of dielectric saturation and is taken as 6. The scaled GMPNP equations for the 3D cylindrical pore is given in the Model details section in the SI.

$$\varepsilon_r = \varepsilon_r^0 \left(\frac{M_{water} - \sum_i^{ncat} w_i C_i}{M_{water}} \right) + \varepsilon_r^{min} \left(\frac{\sum_i^{ncat} w_i C_i}{M_{water}} \right) \tag{21}$$

All species are assumed to be at their bulk concentrations at t=0 with the catalyst in a grounded state as given in equations (22) and (23).

$$C_i|_{x,y,z,t=0} = C_i^0 \tag{22}$$

$$\phi|_{x,y,z,t=0} = 0 \tag{23}$$

The FEniCS project[69,70] Python package is used to solve the Galerkin (weak) form of the GMPNP equations (17) - (20) using backward Euler method for time discretization (details in the SI) over a uniform 3D cylindrical mesh.

Since we are modeling an effective catalyst pore, the current density used for the simulations should be understood as electrochemically active surface area (ECSA)-normalized current density (I_{ECSA}) and not geometrically normalized (I_{geom}). Comparing and bench-

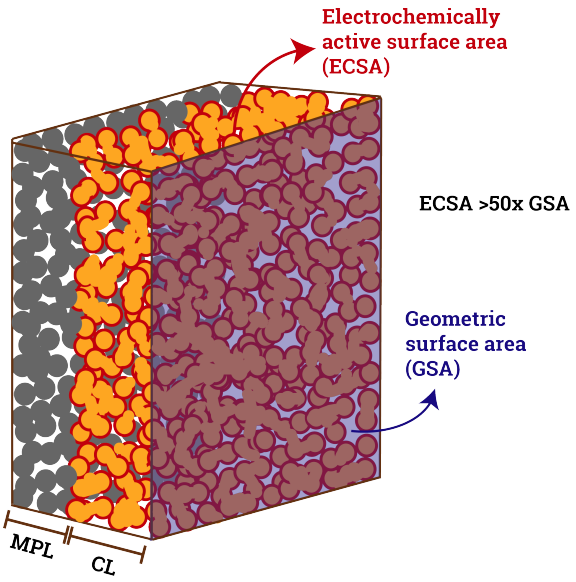

(a)

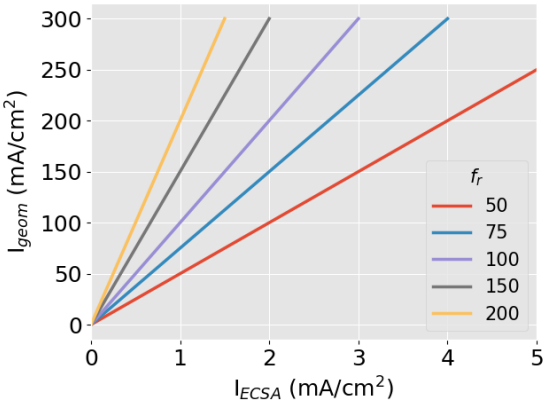

(b)

Figure 2: (a) A cartoon illustration comparing the electrochemically active surface area (ECSA) depicted through the red outlines on the yellow catalyst *vs.* the geometric surface area (GSA) depicted through the blue semi-opaque projected surface on top of the catalyst layer. The grey particles represent the MPL deposited on top of the GDL as shown in Figure 1a. (b) Plot showing geometrically normalized current density (I_{geom}) as a function of the electrochemically active surface area-normalized current density I_{ECSA} for different values of the roughness factor (f_r) as per equation (24).

marking the performance of nanostructured and porous electrodes for electrocatalysis necessitates the estimation of I_{ECSA} through catalytically active surface area measurements.[71–73] Figure 2a illustrates the difference between the catalyst surface area relevant for estimating I_{ECSA} *vs.* I_{geom}. I_{ECSA} can be understood in terms of I_{geom} and the catalyst roughness factor (f_r) as given by equation (24).

$$I_{ECSA} = \frac{I_{geom}}{f_r} \tag{24}$$

McLaughlin et al.[58] have recently reported surface area measurements for Ag GDE which are equivalent to a roughness factor of ~ 50. f_r will depend on the properties of the catalyst and the GDL/MPL layer as well as on the deposition technique and the CL thickness. Additionally, the roughness can also change due to restructuring of the catalyst during op-

eration. We use I_{ECSA} values of 1 mA/cm^2, 2 mA/cm^2 and 3 mA/cm^2 for the simulations in this report. Figure 2b shows I_{geom} as a function of I_{ECSA} with f_r as the slope (equation (24)), highlighting that I_{ECSA} values of 1-3 mA/cm^2 represent experimental geometric current densities in the 100's of mA/cm^2, on par with recent literature.

In the following section, we present the results for GMPNP simulations within a cylindrical pore for changing pore geometry and boundary conditions. Unlike the 1D GMPNP simulations reported in reference 43, where a wide range of potentials were simulated to study the effect on the electrical double layer (EDL), here we focus on comparing the median values of species concentrations within the catalytic pore. The 3D simulations are numerically unstable beyond a small applied potential (V_{app}) at the OHP of -25 mV vs potential at the point of zero charge (PZC) and require extremely small time steps to converge. This makes the simulations at higher V_{app} computationally intractable. All GMPNP results reported in this article are derived for an applied potential of -25 mV vs PZC which corresponds to a surface potential of $\sim$ -0.5 V vs standard hydrogen electrode (SHE) for Ag(111) and $\sim$ -0.75 V vs SHE for polycrystalline Ag (see Parameters section in the SI). Steric effects are not expected to play an important role at small applied potentials and similar results are expected from a PNP model without any steric modifications to the flux term in equation (18). However, the GMPNP equations are numerically more stable than PNP and do not require additional numerical stabilization for convergence Bohra et al..[43]

Lastly, based on the few attempts at measuring the pore structure properties of metal catalysts deposited on GDEs for eCO_2R,[22,58] the pore radii are expected to lie between 100 to 1000 nm. We have assumed a radius of 5 nm for our simulations unless otherwise stated, primarily due to computational limitations since the finite element mesh grows with R^2. A very fine space discretization is needed in order to resolve the EDL region close to the cylindrical surface S_2 using the GMPNP model. A mesh with radially variable element sizes can be used for pores with larger radii to circumvent this issue. The pore radius is not expected to influence the conclusions drawn regarding the influence of pore structure on

mean reaction conditions within the pore. However, the influence of R will become prominent when studying the effect of applied potential on median reaction conditions within the pore and will be discussed further in the results section.

Results

In the following section, we vary different aspects of the pore structure to study its effect on the median properties of the electrolyte within the effective catalyst pore. Subsequently, we consider the effect of the model choices such as the boundary conditions in more detail and provide a comparison with the reaction-diffusion model.

Pore structure of catalyst

Length of catalyst pore

The length of the catalyst pore is a function of the thickness of the catalyst layer deposited on top of the MPL as well as the tortuosity (τ) of the porous structure. We have varied the length of the model cylindrical pore L in order to study its effect on the concentration of the various solution species within the pore. Catalyst layer thickness has been shown to effect the eCO_2R performance experimentally where the variation has been attributed to CO_2 concentration and the pH within the catalyst pores.[27]

Figure 3a and 3b show how, as the length of the pore increases, the pH in the pore becomes more basic accompanied by a buffer breakdown seen by the depletion of HCO_3^- from the pore. This dramatic increase in pH for constant I_{ECSA} with increasing L is a result of the relative rate of diffusion of species within the pore and their flux at the electrolyte-electrolyte interface S_3. The length of the pore needed for the buffer breakdown to happen goes down with increasing I_{ECSA} due to a higher rate of OH^- production. Another interesting consequence of increasing pore length is the build-up of cations and carbonate ions within

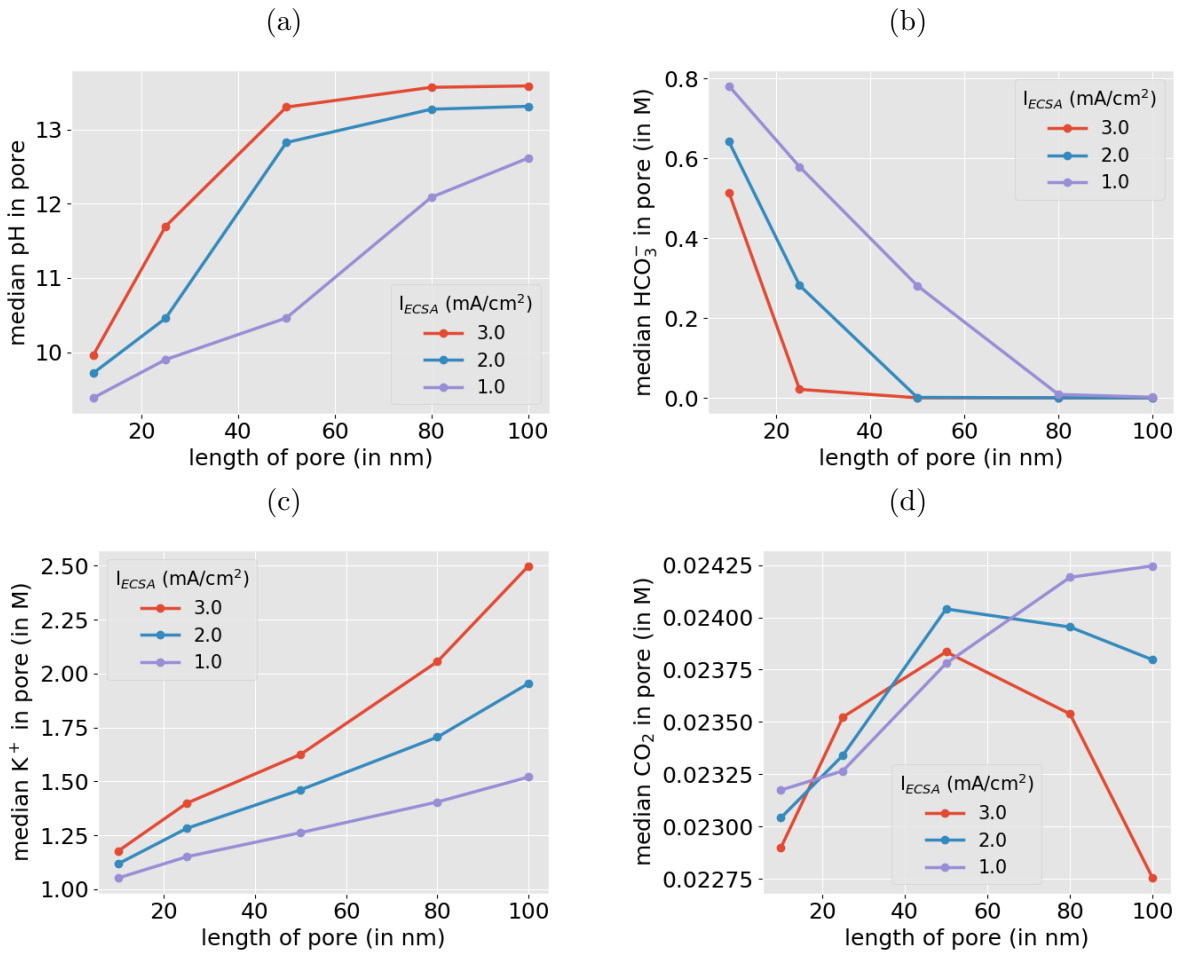

Figure 3: Influence of changing length (L) of effective catalyst pore on median concentrations of electrolyte species within pore for different values of I_{ECSA}. Figure 2b and equation (24) can be used to translate the I_{ECSA} values to the corresponding I_{geom} and roughness factor (f_r). The radius (R) of all pores is 5 nm.

the pore as can be seen in Figure 3c and S1. The concentration of these charged species has an influence on the solubility of CO_2 within the pore as described in the model description section. The concentration of the cations and carbonate ions can also be relevant for ion precipitation within the catalyst pores which can potentially lead to fouling.[22,31] We do not assume any specific adsorption of cations on the catalyst surface in our simulations. However, an increased build-up of cations within the pores at high applied voltage can possibly result in the cations chemically adsorbing on the catalyst walls and significantly influencing catalyst activity. Although, the absolute CO_2 concentration does not change significantly over the

whole range of L and I_{ECSA} (Figure 3d), the trend shows a clear competition between the outgoing CO_2 fluxes at S_2 and S_3 as well as the influence of higher ion concentrations on the equilibrium concentration of CO_2 at S_1.

Figures 8b, S7b, S9a, S8b and S10 show the distribution of electrolyte species across a longitudinal cross-section of a 5 nm x 100 nm (R x L) pore derived for the GMPNP model. No significant variation can be observed for the solution species along the length of the pore except for the products CO and H_2 which are present in a very low concentration. The species fluxes and the applied potential, however, have a clear influence on the concentration profiles along the pore boundaries. The influence of applied potential on concentration profiles follows the same general behavior as discussed in reference 43. The product gases CO and H_2 are assumed to be at equilibrium at the gas-liquid interface as mentioned previously. This implies that as the catalytic reaction progresses within the pore, CO and H_2 build up beyond their equilibrium solution concentration along the length of the pore as can be seen in Figure S10. The mass transport of gaseous product species from the flooded catalyst pore through the GDL can be much more complex than captured by the model used. However, since CO and H_2 are present in very low concentrations, are uncharged species and do not participate in any homogeneous reactions in the electrolyte, their mass transport within the pore can be independently resolved through more complex models that take into account possible nucleation and bubble formation. If the formation of gaseous bubbles is, in fact, a significant effect within the catalyst pores, this will in turn influence the mass transport of other species through turbulence and fluctuation of catalyst surface voltage[74] leading to a much more complex dependence between the transport and catalyst performance.

Surface area of catalyst pore

Catalyst surface area is often regarded as a very important parameter for improving performance, but the dimension in which surface area is increased is not inconsequential. Figure 4 compares the concentration of electrolyte species for catalyst pores having the same surface

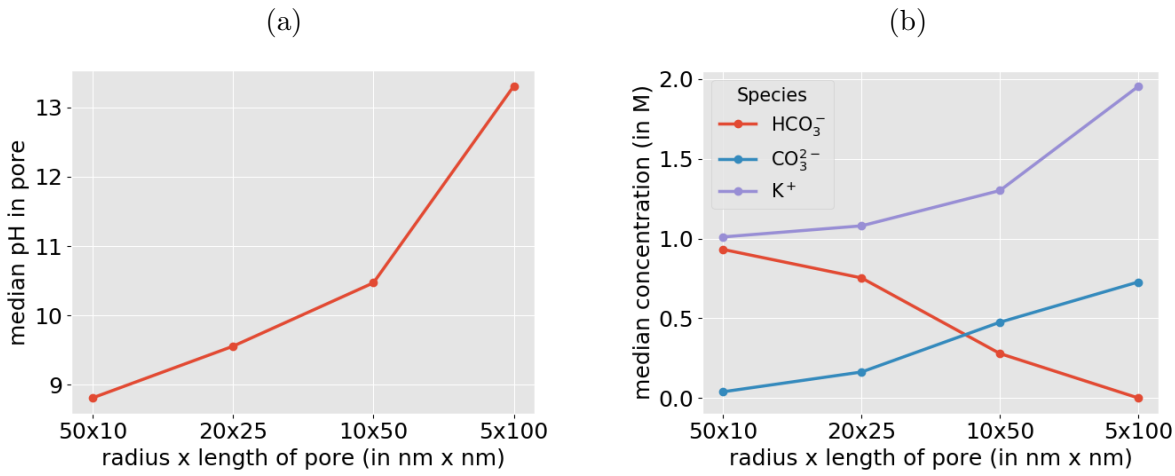

Figure 4: Comparison of median concentration of electrolyte species within catalyst pore for pores with same surface area. Results derived at I_{ECSA}=2 mA/cm^2.

area but different proportions of R and L. It can be seen that even for the same surface area and I_{ECSA}, the difference between the reaction environment within the pores is dramatic. The construction of the GDE flow-cell system is such that a relatively thin catalyst layer faces a gas-liquid interface on one side and electrolyte flowing in a direction perpendicular to the pore length on the other. As a consequence, the thickness of the catalyst layer (L) ends up being the dominant effect and the trend seen in Figure 4 is not very different from the blue curves for I_{ECSA}=2 mA/cm^2 in Figure 3. Therefore, catalysts with the same surface area but with different catalyst layer thickness can be expected to show very different selectivity for CO_2 reduction. Experimentally, identical catalytic materials may then give the appearance of varying catalytic activity when in fact only the orientation may be different.

Geometric vs ECSA normalized current density

Figure 5 and S3 demonstrate the difference between comparing the reaction environment within the catalyst pores at a fixed ECSA *vs.* geometrically normalized current density. I_{geom} is fixed (red dotted curve) such that the I_{ECSA} is 1 mA/cm^2 for a pore of length 100 nm. The roughness factor is assumed to be directly proportional to the pore surface area and the I_{ECSA} is adjusted accordingly to keep I_{ECSA}*f_r or I_{geom} constant (see equation

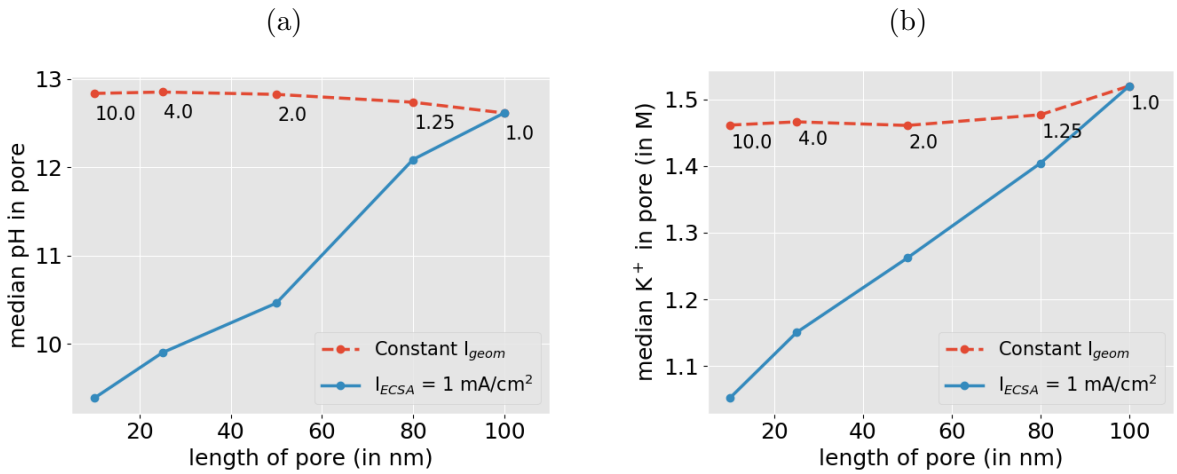

Figure 5: A comparison between median pH and cation concentration within pore derived for constant I_{geom} *vs.* constant I_{ECSA} of 1 mA/cm^2. The annotations on the red dotted curve signify the value of I_{ECSA} corresponding to the respective pore size for the constant I_{geom}. The radius of pore (R) is 5 nm for all cases.

24). The pH or the cation concentration within the pore does not change significantly when compared at constant I_{geom} unlike at a constant I_{ECSA}. However, a comparison of different catalysts at constant I_{geom} is not useful for isolating the influence of the inherent catalytic activity and the reaction environment by not taking into account the active surface area of the catalyst.[71–73] Collectively, these results communicate the challenges associated with interpreting experimental data commonly reported in the form of geometric current density, and comparing data sets performed under varying ECSA current density.

Effective diffusion coefficient in catalyst pore

One of the effects of changing the porous structure of the catalyst is the change in the effective diffusion coefficient of electrolyte species as given by equation (19). For catalyst pores flooded with electrolyte, the ratio of the effective and bulk diffusion coefficient (D^i_{eff}/D^i) for a species can range between 0 and 1. Figure S2 in the SI shows how changing this ratio has no considerable effect on the median reaction environment within the pore. Therefore, it can be concluded that unless the medium of species transport within the pore changes, the change in the effective diffusion coefficient of species with changing catalyst structure is

not an important effect. The effective porosity (ϵ), constrictivity (δ) and tortuosity (τ) are however, influential factors as they are directly related to the catalyst structure.

Boundary conditions and choice of model

The CL thickness is typically in the order of a few 100 nm in a typical GDE based flow-cell, which is small relative to the thickness of a gas-diffusion layer and the electrolyte diffusion layer. Consequently, the boundary conditions at S_1 and S_3 for the CL play a hugely important role in determining the reaction conditions as they act as the entry and exit point of all species. Transport and replenishment in these layers is likely more limiting than within the GDE pores. The following sections discuss the influence of the electrolyte flow rate at the electrolyte-electrolyte-interface S_3, the gas pressure at the gas-electrolyte interface S_1 and the applied potential at the catalyst surface S_2 on the environment within the model pore.

Electrolyte flow rate

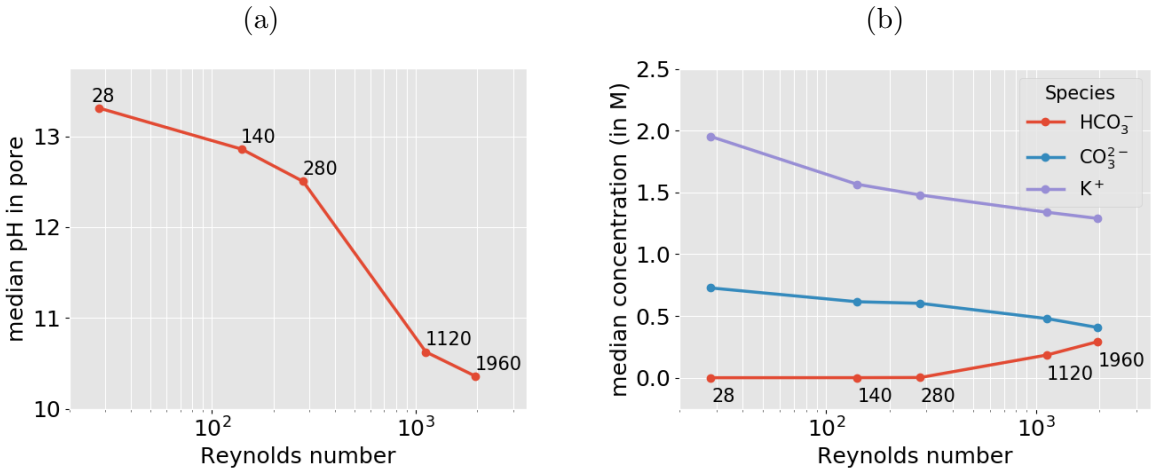

Figure 6: Effect of changing Reynolds number on the median pH and concentration of charged species in the catalyst pore. Reynolds numbers of 28, 140, 280, 1120 and 1960 corresponds to electrolyte flow velocities ($\mid \mathbf{v}_e \mid / A_{cross}$ in equation (14)) of 0.1 m/min, 0.5 m/min, 1 m/min, 4 m/min and 7 m/min, respectively. A pore of 5 nm x 100 nm (R x L) and I_{ECSA}=2 mA/cm^2 is used for all data points.

Figure 6 shows the influence of changing the Reynolds number for the electrolyte flow at the electrolyte-electrolyte interface in a direction perpendicular to the pore length (see Figure 1a). The default Reynolds number according to our typically laboratory setup[75] is calculated to be ~ 28. This is equivalent to an electrolyte flow velocity of 0.1 m/min or a volumetric flow of 15 ml/min ($\mid \mathbf{v}_e \mid$) across a flow channel with cross section of 1.5 cm^2 (A_{cross}) as per equation (14). The Reynolds number for the electrolyte flow influences the flux of species at the interface S_3 according to the equations (12) - (15).

The pH within the catalyst pore reduces dramatically on increasing the Reynolds number as seen in Figure 6a by increasing the flux of OH^- ions out of the pore towards the bulk electrolyte. The red curve for HCO_3^- in Figure 6b follows the pH trend signifying buffer breakdown at low electrolyte flow rates. Although, the CO_2 concentration in the pore does not change significantly due to Reynolds number as shown in Figure S4, the concave nature of the curve demonstrates the competition between CO_2 solubility based on the ionic concentration within the pore and the outward flux of the CO_2 at S_3. Experimentally, flow rate of electrolyte has been shown to influence the catalyst selectivity in experimental studies using flow-cells.[24,29] This is not surprising considering the extent to which electrolyte flow can potentially alter conditions within the CL. Management of pressure drop across the GDE can however, be a non-trivial aspect of the operation of the flow-cell and can possibly limit the use of electrolyte flow rate as a control mechanism for product selectivity.

Gas pressure

Gas pressure has also been used as an operational handle to tune product selectivity in flow-cells.[26] A variation in gas-pressure will need adjustment of the liquid pressure in order to maintain the gas-electrolyte interface at S_1 such that the capillary pressure of the pores plus the liquid pressure balance the gas pressure. A pressure imbalance can lead to either gas channels entering the CL pores or flooding of the GDL, which will significantly change the nature of mass transport within the CL. We assume that S_1 remains stationary after

increasing the gas pressure and that the electrolyte properties remain unchanged.

Figure S5 in the SI shows the influence of increasing pressure at the gas-electrolyte interface S_1 on the reaction environment within the pore. Increasing the gas pressure from 1 bar to 10 bar leads to a reduction in the pH by ~ 0.8 units and factor of 10 increase in the median CO_2 concentration. The reduction of pH on increasing gas pressure also results in an increase in CO_3^{2-} and K^+ as a consequence of the buffer reactions and the electrostatic interactions in the electrolyte. In terms of pH, the effect of increasing the gas pressure by a factor of 10 is very similar to the effect of reducing the electrolyte flow velocity by a factor of 10 at the electrolyte-electrolyte interface (see drop in pH between a Reynolds number of 28 and 280 in Figure 6a). The influence on the CO_2 availability within the pore however, is very different for the two scenarios. Both operational handles of gas pressure and electrolyte flow involve practical challenges regarding management of flooding of the GDL and electrolyte distribution within the CL. The appropriate control mechanism for reaction conditions can be chosen based on whether CO_2 concentration becomes limiting through the CL (for thick layers) and the stability of the gas-electrolyte interface.

Applied potential

We compare the output from a reaction diffusion model (model details in the SI) with the GMPNP model to understand the influence of taking applied potential at the catalyst surface S_2 into account. A reaction-diffusion model does not take electrostatic effects of the system and reaction interface into account, and will thus lead to different steady-state concentrations of species within the GDE pore as compared to the GMPNP model.

For the small pore radius of 5 nm and a small applied potential of -25 mV vs PZC used as a boundary condition for the GMPNP model, the median pH (Figure 7a) and buffer breakdown (Figure S6) with changing pore length does not vary significantly between the two models. This is not surprising, since the effect of the EDL formation is restricted to

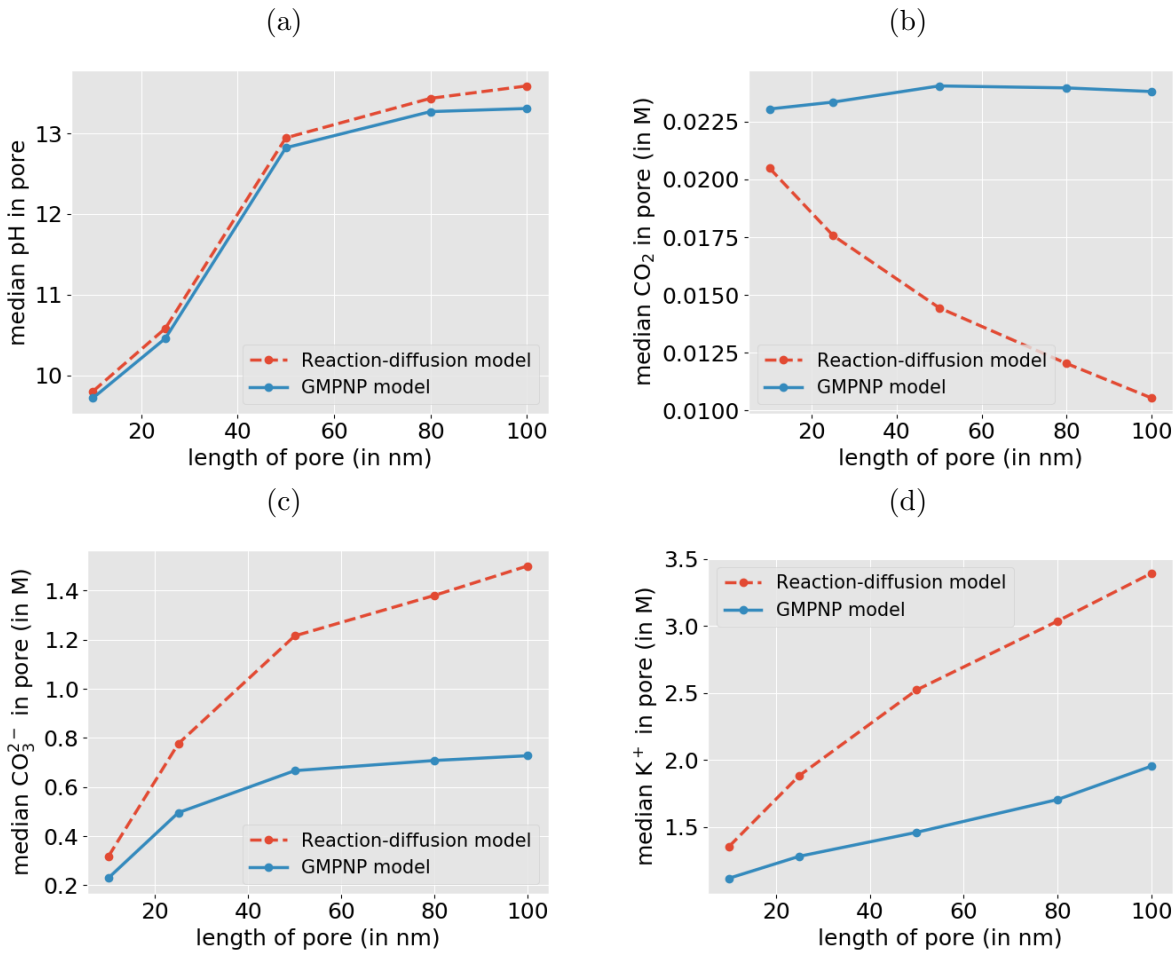

Figure 7: Comparing the median concentration of species in the catalyst pore with changing pore length (L) derived using a reaction-diffusion model and a GMPNP model. A pore of 5 nm x 100 nm (R x L) and I_{ECSA}=2 mA/cm^2 is used for all data points.

$\sim$ 1 nm around the catalyst surface at the small applied potential and is not expected to perturb the median H^+ concentration of the pore drastically. The slightly low pH obtained for GMPNP is owing to the fact that the catalyst surface is negatively charged leading to a build-up of positively charged ions in the EDL.

Comparing the predicted CO_3^{2-} and K^+ concentrations between the two models, however, a much larger discrepancy is observed. In the reaction diffusion model the ion concentrations are predicted to be much higher than in the case of the GMPNP model (Figures 7c and 7d). The model differences are a result of the applied electric field in the GMPNP model which drives the repulsion of CO_3^{2-} from the GDE pore, leading to an overall different

balance of charged species versus the reaction-diffusion model. Critically, this variation in-turn influences the solubility of CO_2 in the electrolyte and results in the deviating trends seen for median CO_2 concentration in Figure 7b.

(a) Common scale

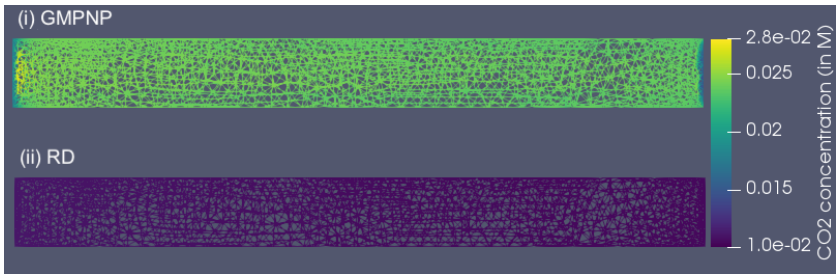

(b) GMPNP

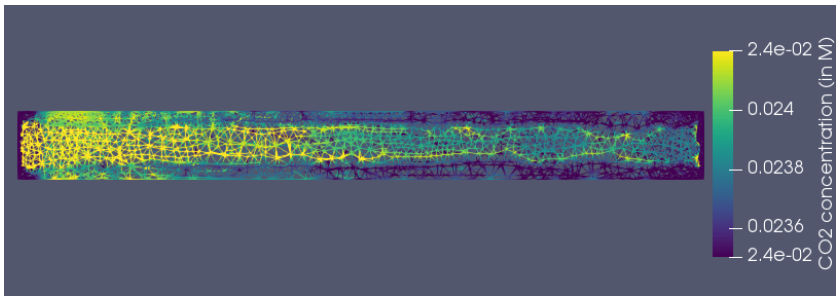

(c) RD

Figure 8: A comparison of CO_2 concentration along a longitudinal cross-section of a pore with R x L of 5 nm x 100 nm and I_{ECSA}=2 mA/cm^2 for the GMPNP and reaction-diffusion (RD) model. An applied potential of -25 mV vs PZC for the catalyst surface is used for the GMPNP model. The gas-liquid interface is the left edge whereas the electrolyte-electrolyte interface is the right edge with the top and bottom edges being part of the catalyst surface. (a) shows the output of the GMPNP and RD model on the same scale for comparison. (b) and (c) show the distribution on separate scales for clarity.

Figure 8 shows the spatial CO_2 concentration along a longitudinal cross-section of the pore. The concentration of CO_2 does not vary significantly within the pore for either of the models as can be seen from Figure 8a. However, making the concentration scales narrower

for each model reveals a very different distribution of CO_2, both radially and longitudinally. The concentration profile obtained using the GMPNP model in Figure 8b clearly captures the edge effects due to the presence of the electric field at the catalyst surface as well as ion accumulation in the EDL which are absent in the reaction-diffusion model in Figure 8a. Similar comparisons for other solution species can be found in Figures S7b, S9a, S8b and S10 in the SI.

Increasing the radius of the pore is expected to diminish the influence of the EDL on the median concentration predicted by the GMPNP. On the other hand, a higher applied potential should further exaggerate the differences in the prediction from the GMPNP *vs.* the reaction-diffusion model. Using the reaction-diffusion model to derive trends for median reaction conditions in the pore volume can be a reasonable choice, especially when studying pores with large radii and lengths. However, if it is desired to study the edge effects in these systems such as the environment in the vicinity of the interfaces, the reaction-diffusion model can be grossly insufficient owing to the missing electrostatic effects.

Lastly, it is worth noting that the curvature of pores with >= 5 nm radius is expected to be large enough for the EDL to behave similar to a flat plate and 1D simulations such as presented in reference 43 can instead be used to specifically study the EDL properties.[76] The arrangement of ions within pores with radii similar in length scale to the EDL can no longer be accurately predicted using continuum models and requires molecular level treatment.[77–79] Pores with high curvature (small radii) can make the limitations of the current GMPNP model even more pronounced, especially regarding the treatment of solvent water molecules and their relative interaction with the hydrophilic catalyst surface *vs.* the ionic species, van der Waals forces and Coulombic interaction between charged species.[80] It is not expected for pores below 5 nm radius to have a significant population in the CL and therefore can be safely ignored for building models for the CL.[22,58]

Conclusions

An effective flooded cylindrical catalyst pore was used to study the influence of changing pore geometry and boundary conditions on the reaction environment during eCO_2R in a GDE-based flow cell setup. The length of the catalytic pore was found to be an important parameter, determining the pH, buffer breakdown and concentration of ionic species in the pore. We find that pores with the same surface area but different lengths can have very different reaction environments. The thickness of the deposited catalyst layer on top of the GDL is therefore expected to be an important design handle for optimizing performance. The flux of species across the gas-electrolyte interface at the MPL/CL boundary as well as across the electrolyte-electrolyte interface also play a significant role in determining the reaction conditions within the CL. The transport properties and operating conditions for the gas flow, the gas composition and pressure, and the electrolyte flow rate and flow-channel geometry, are therefore expected to have a major influence on the resultant catalyst selectivity and activity. A comparison of the GMPNP model with the reaction-diffusion model shows that the applied potential is an important parameter for ionic concentration within the pore, which in turn influences the CO_2 solubility in the electrolyte. Reaction-diffusion model can be sufficient for studying median concentration of species within the catalyst layer for pores with large radii and length since the influence of the relatively thin electrical double layer (EDL) diminishes with the increasing pore volume. However, considering the electrostatic effect of the applied potential becomes essential if studying edge effects and the environment in the vicinity of the catalyst surface is the aim.

Management of pressure drop across the various system components to maintain the desired gas-electrolyte interfaces for catalysis can be very challenging for practical operation of flow-cell systems. There is a need to better understand the wetting properties of the catalyst layer and the parameters influencing flooding, film thickness and formation of vapor channels in this layer. Fluid dynamics is therefore an important aspect of flow-cell

systems and should be coupled with the PNP equations to model the transport and possible two-phase flow within the CL. Lastly, a major challenge in modeling heterogeneous porous catalytic systems lies in the upscaling of microscopic models such as the one reported here to the macroscopic level.[81] Developing upscaling frameworks to accurately model the influential aspects of the mass transport will be an important step to study the performance of GDE-based eCO_2R systems. The presence of 2-phase interfaces and electrolyte flow at the boundaries of a relatively thin, charged and nanostructured catalyst layer, make mass transport central to the performance of flow-cell setups for eCO_2R. The sensitivity of the catalysis to structural and operational parameters for such systems will be significantly higher than the traditionally studied H-cells. The field should therefore move towards benchmarking of system performance against these parameters to improve reproducibility and shorten the development cycle towards an industrial scale system.

Acknowledgement

This project received funding from NWO via the VIDI grant (WAS and DB). The authors thank Dr Nathan Nesbitt for valuable discussions during the course of this research.

Supporting Information Available

Supporting modeling details, parameter values and simulation results available.

References

(1) Zhang, W.; Hu, Y.; Ma, L.; Zhu, G.; Wang, Y.; Xue, X.; Chen, R.; Yang, S.; Jin, Z. Progress and Perspective of Electrocatalytic CO_2 Reduction for Renewable Carbonaceous Fuels and Chemicals. *Advanced Science* **2018**, *5*, 1700275.

(2) Zhang, L.; Wang, Z.; Mehio, N.; Jin, X.; Dai, S. Thickness- and Particle-Size-Dependent

Electrochemical Reduction of Carbon Dioxide on Thin-Layer Porous Silver Electrodes. *ChemSusChem* **2016**, *9*, 428–432.

(3) Lu, Q.; Rosen, J.; Zhou, Y.; Hutchings, G. S.; Kimmel, Y. C.; Chen, J. G.; Jiao, F. A selective and efficient electrocatalyst for carbon dioxide reduction. *Nature Communications* **2014**, *5*, 3242.

(4) Li, F.; Zhao, S.-F.; Chen, L.; Khan, A.; MacFarlane, D. R.; Zhang, J. Polyethylenimine promoted electrocatalytic reduction of CO_2 to CO in aqueous medium by graphene-supported amorphous molybdenum sulphide. *Energy Environ. Sci.* **2016**, *9*, 216–223.

(5) Kim, S. K.; Zhang, Y.-J.; Bergstrom, H.; Michalsky, R.; Peterson, A. Understanding the Low-Overpotential Production of CH_4 from CO_2 on Mo_2C Catalysts. *ACS Catalysis* **2016**, *6*, 2003–2013.

(6) Li, F.; Chen, L.; Knowles, G. P.; MacFarlane, D. R.; Zhang, J. Hierarchical mesoporous SnO_2 nanosheets on carbon cloth: a robust and flexible electrocatalyst for CO_2 reduction with high efficiency and selectivity. *Angewandte chemie international edition* **2017**, *56*, 505–509.

(7) Luc, W.; Collins, C.; Wang, S.; Xin, H.; He, K.; Kang, Y.; Jiao, F. Ag-Sn Bimetallic Catalyst with a Core-Shell Structure for CO_2 Reduction. *Journal of the American Chemical Society* **2017**, *139*, 1885–1893.

(8) He, J.; Liu, X.; Liu, H.; Zhao, Z.; Ding, Y.; Luo, J. Highly selective electrocatalytic reduction of CO_2 to formate over Tin(IV) sulfide monolayers. *Journal of Catalysis* **2018**, *364*, 125 – 130.

(9) Reske, R.; Mistry, H.; Behafarid, F.; Roldan Cuenya, B.; Strasser, P. Particle Size Effects in the Catalytic Electroreduction of CO_2 on Cu Nanoparticles. *Journal of the American Chemical Society* **2014**, *136*, 6978–6986.

(10) Ren, D.; Deng, Y.; Handoko, A. D.; Chen, C. S.; Malkhandi, S.; Yeo, B. S. Selective Electrochemical Reduction of Carbon Dioxide to Ethylene and Ethanol on Copper(I) Oxide Catalysts. *ACS Catalysis* **2015**, *5*, 2814–2821.

(11) Yang, H.-P.; Qin, S.; Yue, Y.-N.; Liu, L.; Wang, H.; Lu, J.-X. Entrapment of a pyridine derivative within a copper-palladium alloy: a bifunctional catalyst for electrochemical reduction of CO_2 to alcohols with excellent selectivity and reusability. *Catal. Sci. Technol.* **2016**, *6*, 6490–6494.

(12) Jouny, M.; Luc, W.; Jiao, F. General Techno-Economic Analysis of CO_2 Electrolysis Systems. *Industrial & Engineering Chemistry Research* **2018**, *57*, 2165–2177.

(13) Verma, S.; Kim, B.; Jhong, H.-R.; Ma, S.; Kenis, P. J. A. A Gross-Margin Model for Defining Technoeconomic Benchmarks in the Electroreduction of CO_2. *ChemSusChem* **2016**, *9*, 1972–1979.

(14) Spurgeon, J. M.; Kumar, B. A comparative technoeconomic analysis of pathways for commercial electrochemical CO_2 reduction to liquid products. *Energy Environ. Sci.* **2018**, *11*, 1536–1551.

(15) Burdyny, T.; Smith, W. A. CO_2 reduction on gas-diffusion electrodes and why catalytic performance must be assessed at commercially-relevant conditions. *Energy Environ. Sci.* **2019**, *12*, 1442–1453.

(16) Higgins, D.; Hahn, C.; Xiang, C.; Jaramillo, T. F.; Weber, A. Z. Gas-Diffusion Electrodes for Carbon Dioxide Reduction: A New Paradigm. *ACS Energy Letters* **2019**, *4*, 317–324.

(17) Weekes, D. M.; Salvatore, D. A.; Reyes, A.; Huang, A.; Berlinguette, C. P. Electrolytic CO_2 Reduction in a Flow Cell. *Accounts of Chemical Research* **2018**, *51*, 910–918.

(18) Fan, L.; Xia, C.; Yang, F.; Wang, J.; Wang, H.; Lu, Y. Strategies in catalysts and electrolyzer design for electrochemical CO_2 reduction toward C_{2+} products. *Science Advances* **2020**, *6*.

(19) Sánchez, O. G.; Birdja, Y. Y.; Bulut, M.; Vaes, J.; Breugelmans, T.; Pant, D. Recent advances in industrial CO_2 electroreduction. *Current Opinion in Green and Sustainable Chemistry* **2019**, *16*, 47 – 56, CO2 Capture and Chemistry.

(20) Kibria, M. G.; Edwards, J. P.; Gabardo, C. M.; Dinh, C.-T.; Seifitokaldani, A.; Sinton, D.; Sargent, E. H. Electrochemical CO_2 reduction into chemical feedstocks: from mechanistic electrocatalysis models to system design. *Advanced Materials* **2019**, *31*, 1807166.

(21) Endrődi, B.; Bencsik, G.; Darvas, F.; Jones, R.; Rajeshwar, K.; Janáky, C. Continuous-flow electroreduction of carbon dioxide. *Progress in Energy and Combustion Science* **2017**, *62*, 133 – 154.

(22) Lv, J.-J.; Jouny, M.; Luc, W.; Zhu, W.; Zhu, J.-J.; Jiao, F. A Highly Porous Copper Electrocatalyst for Carbon Dioxide Reduction. *Advanced Materials* **2018**, *30*, 1803111.

(23) Wu, J. et al. A metal-free electrocatalyst for carbon dioxide reduction to multi-carbon hydrocarbons and oxygenates. *Nature Communications* **2016**, *7*, 13869.

(24) Delacourt, C.; Ridgway, P. L.; Kerr, J. B.; Newman, J. Design of an Electrochemical Cell Making Syngas ($CO+H_2$) from CO_2 and H_2O Reduction at Room Temperature. *Journal of The Electrochemical Society* **2008**, *155*, B42.

(25) Verma, S.; Lu, X.; Ma, S.; Masel, R. I.; Kenis, P. J. A. The effect of electrolyte composition on the electroreduction of CO_2 to CO on Ag based gas diffusion electrodes. *Phys. Chem. Chem. Phys.* **2016**, *18*, 7075–7084.

(26) Gabardo, C. M.; Seifitokaldani, A.; Edwards, J. P.; Dinh, C.-T.; Burdyny, T.; Kibria, M. G.; O'Brien, C. P.; Sargent, E. H.; Sinton, D. Combined high alkalinity and pressurization enable efficient CO_2 electroreduction to CO. *Energy & Environmental Science* **2018**, *11*, 2531–2539.

(27) Dinh, C.-T.; Burdyny, T.; Kibria, M. G.; Seifitokaldani, A.; Gabardo, C. M.; De Arquer, F. P. G.; Kiani, A.; Edwards, J. P.; De Luna, P.; Bushuyev, O. S., et al. CO_2 electroreduction to ethylene via hydroxide-mediated copper catalysis at an abrupt interface. *Science* **2018**, *360*, 783–787.

(28) Kibria, M. G.; Dinh, C.-T.; Seifitokaldani, A.; De Luna, P.; Burdyny, T.; Quintero-Bermudez, R.; Ross, M. B.; Bushuyev, O. S.; García de Arquer, F. P.; Yang, P.; Sinton, D.; Sargent, E. H. A Surface Reconstruction Route to High Productivity and Selectivity in CO_2 Electroreduction toward C^{2+} Hydrocarbons. *Advanced Materials* **2018**, *30*, 1804867.

(29) Whipple, D. T.; Finke, E. C.; Kenis, P. J. A. Microfluidic Reactor for the Electrochemical Reduction of Carbon Dioxide: The Effect of pH. *Electrochemical and Solid-State Letters* **2010**, *13*, B109.

(30) Li, H.; Oloman, C. The electro-reduction of carbon dioxide in a continuous reactor. *Journal of Applied Electrochemistry* **2005**, *35*, 955–965.

(31) Verma, S.; Hamasaki, Y.; Kim, C.; Huang, W.; Lu, S.; Jhong, H.-R. M.; Gewirth, A. A.; Fujigaya, T.; Nakashima, N.; Kenis, P. J. A. Insights into the Low Overpotential Electroreduction of CO2 to CO on a Supported Gold Catalyst in an Alkaline Flow Electrolyzer. *ACS Energy Letters* **2018**, *3*, 193–198.

(32) Li, Y. C.; Zhou, D.; Yan, Z.; Gonçalves, R. H.; Salvatore, D. A.; Berlinguette, C. P.; Mallouk, T. E. Electrolysis of CO_2 to Syngas in Bipolar Membrane-Based Electrochemical Cells. *ACS Energy Letters* **2016**, *1*, 1149–1153.

(33) Liu, Z.; Masel, R. I.; Chen, Q.; Kutz, R.; Yang, H.; Lewinski, K.; Kaplun, M.; Luopa, S.; Lutz, D. R. Electrochemical generation of syngas from water and carbon dioxide at industrially important rates. *Journal of CO2 Utilization* **2016**, *15*, 50 – 56.

(34) Lee, W.; Kim, Y. E.; Youn, M. H.; Jeong, S. K.; Park, K. T. Catholyte-Free Electrocatalytic CO2 Reduction to Formate. *Angewandte Chemie International Edition* **2018**, *57*, 6883–6887.

(35) Zheng, T.; Jiang, K.; Ta, N.; Hu, Y.; Zeng, J.; Liu, J.; Wang, H. Large-Scale and Highly Selective CO_2 Electrocatalytic Reduction on Nickel Single-Atom Catalyst. *Joule* **2019**, *3*, 265 – 278.

(36) Gabardo, C. M.; O'Brien, C. P.; Edwards, J. P.; McCallum, C.; Xu, Y.; Dinh, C.-T.; Li, J.; Sargent, E. H.; Sinton, D. Continuous carbon dioxide electroreduction to concentrated multi-carbon products using a membrane electrode assembly. *Joule* **2019**, *3*, 2777–2791.

(37) Xia, C.; Zhu, P.; Jiang, Q.; Pan, Y.; Liang, W.; Stavitski, E.; Alshareef, H. N.; Wang, H. Continuous production of pure liquid fuel solutions via electrocatalytic CO_2 reduction using solid-electrolyte devices. *Nature Energy* **2019**, *4*, 776–785.

(38) Yin, Z.; Peng, H.; Wei, X.; Zhou, H.; Gong, J.; Huai, M.; Xiao, L.; Wang, G.; Lu, J.; Zhuang, L. An alkaline polymer electrolyte CO_2 electrolyzer operated with pure water. *Energy Environ. Sci.* **2019**, *12*, 2455–2462.

(39) de Arquer, F. P. G.; Dinh, C.-T.; Ozden, A.; Wicks, J.; McCallum, C.; Kirmani, A. R.; Nam, D.-H.; Gabardo, C.; Seifitokaldani, A.; Wang, X., et al. CO_2 electrolysis to multicarbon products at activities greater than 1 A cm^{-2}. *Science* **2020**, *367*, 661–666.

(40) De Mot, B.; Ramdin, M.; Hereijgers, J.; Vlugt, T. J. H.; Breugelmans, T. Direct Water Injection in Catholyte-Free Zero-Gap Carbon Dioxide Electrolyzers. *ChemElectroChem* **2020**, *7*, 3839–3843.

(41) Larrazábal, G. O.; Strøm-Hansen, P.; Heli, J. P.; Zeiter, K.; Therkildsen, K. T.; Chorkendorff, I.; Seger, B. Analysis of mass flows and membrane cross-over in CO2 reduction at high current densities in an MEA-type electrolyzer. *ACS applied materials & interfaces* **2019**, *11*, 41281–41288.

(42) Weekes, D. M.; Salvatore, D. A.; Reyes, A.; Huang, A.; Berlinguette, C. P. Electrolytic CO2 reduction in a flow cell. *Accounts of chemical research* **2018**, *51*, 910–918.

(43) Bohra, D.; Chaudhry, J. H.; Burdyny, T.; Pidko, E. A.; Smith, W. A. Modeling the electrical double layer to understand the reaction environment in a CO_2 electrocatalytic system. *Energy Environ. Sci.* **2019**, *12*, 3380–3389.

(44) Gupta, N.; Gattrell, M.; MacDougall, B. Calculation for the cathode surface concentrations in the electrochemical reduction of CO_2 in $KHCO_3$ solutions. *Journal of Applied Electrochemistry* **2006**, *36*, 161–172.

(45) Suter, S.; Haussener, S. Optimizing mesostructured silver catalysts for selective carbon dioxide conversion into fuels. *Energy Environ. Sci.* **2019**, *12*, 1668–1678.

(46) Liu, M. et al. Enhanced electrocatalytic CO_2 reduction via field-induced reagent concentration. *Nature* **2016**, *537*, 382 EP –.

(47) Resasco, J.; Chen, L. D.; Clark, E.; Tsai, C.; Hahn, C.; Jaramillo, T. F.; Chan, K.; Bell, A. T. Promoter Effects of Alkali Metal Cations on the Electrochemical Reduction of Carbon Dioxide. *Journal of the American Chemical Society* **2017**, *139*, 11277–11287.

(48) Larrazábal, G. O.; Martín, A. J.; Pérez-Ramírez, J. Building Blocks for High Performance in Electrocatalytic CO_2 Reduction: Materials, Optimization Strategies, and Device Engineering. *The Journal of Physical Chemistry Letters* **2017**, *8*, 3933–3944.

(49) Varela, A. S.; Kroschel, M.; Reier, T.; Strasser, P. Controlling the selectivity of CO_2 electroreduction on copper: The effect of the electrolyte concentration and the im-

portance of the local pH. *Catalysis Today* **2016**, *260*, 8 – 13, Surface Analysis and Dynamics (SAND).

(50) Kas, R.; Kortlever, R.; Yilmaz, H.; Koper, M. T. M.; Mul, G. Manipulating the Hydrocarbon Selectivity of Copper Nanoparticles in CO_2 Electroreduction by Process Conditions. *ChemElectroChem* **2015**, *2*, 354–358.

(51) Ma, M.; Djanashvili, K.; Smith, W. A. Controllable Hydrocarbon Formation from the Electrochemical Reduction of CO_2 over Cu Nanowire Arrays. *Angewandte Chemie International Edition* **2016**, *55*, 6680–6684.

(52) Ma, M.; Trześniewski, B. J.; Xie, J.; Smith, W. A. Selective and Efficient Reduction of Carbon Dioxide to Carbon Monoxide on Oxide-Derived Nanostructured Silver Electrocatalysts. *Angewandte Chemie International Edition* **2016**, *55*, 9748–9752.

(53) Weng, L.-C.; Bell, A. T.; Weber, A. Z. Modeling gas-diffusion electrodes for CO_2 reduction. *Phys. Chem. Chem. Phys.* **2018**, *20*, 16973–16984.

(54) Wu, K.; Birgersson, E.; Kim, B.; Kenis, P. J.; Karimi, I. A. Modeling and experimental validation of electrochemical reduction of CO_2 to CO in a microfluidic cell. *Journal of The Electrochemical Society* **2015**, *162*, F23–F32.

(55) Giner, J.; Hunter, C. The Mechanism of Operation of the Teflon-Bonded Gas Diffusion Electrode: A Mathematical Model. *Journal of The Electrochemical Society* **1969**, *116*, 1124.

(56) Kilic, M. S.; Bazant, M. Z.; Ajdari, A. Steric effects in the dynamics of electrolytes at large applied voltages. II. Modified Poisson-Nernst-Planck equations. *Phys. Rev. E* **2007**, *75*, 021503.

(57) Wang, H.; Thiele, A.; Pilon, L. Simulations of Cyclic Voltammetry for Electric Dou-

ble Layers in Asymmetric Electrolytes: A Generalized Modified Poisson-Nernst-Planck Model. *The Journal of Physical Chemistry C* **2013**, *117*, 18286–18297.

(58) McLaughlin, D.; Bierling, M.; Moroni, R.; Vogl, C.; Schmid, G.; Thiele, S. Tomographic Reconstruction and Analysis of a Silver CO_2 Reduction Cathode. *Advanced Energy Materials* **2020**, *n/a*, 2000488.

(59) Haas, T.; Krause, R.; Weber, R.; Demler, M.; Schmid, G. Technical photosynthesis involving CO_2 electrolysis and fermentation. *Nature Catalysis* **2018**, *1*, 32–39.

(60) Verma, S.; Hamasaki, Y.; Kim, C.; Huang, W.; Lu, S.; Jhong, H.-R. M.; Gewirth, A. A.; Fujigaya, T.; Nakashima, N.; Kenis, P. J. Insights into the low overpotential electroreduction of CO_2 to CO on a supported gold catalyst in an alkaline flow electrolyzer. *ACS Energy Letters* **2017**, *3*, 193–198.

(61) Ma, S.; Luo, R.; Gold, J. I.; Aaron, Z. Y.; Kim, B.; Kenis, P. J. Carbon nanotube containing Ag catalyst layers for efficient and selective reduction of carbon dioxide. *Journal of Materials Chemistry A* **2016**, *4*, 8573–8578.

(62) Dufek, E. J.; Lister, T. E.; Stone, S. G.; McIlwain, M. E. Operation of a pressurized system for continuous reduction of CO_2. *Journal of The Electrochemical Society* **2012**, *159*, F514.

(63) Bird, R. B.; Stewart, W. E.; Lightfoot, E. N. *Transport Phenomena, Revised 2nd Edition*; Wiley, 2006; pp 671–725.

(64) Weisenberger, S.; Schumpe, A. Estimation of gas solubilities in salt solutions at temperatures from 273 K to 363 K. *AIChE Journal* **1996**, *42*, 298–300.

(65) Burdyny, T.; Graham, P. J.; Pang, Y.; Dinh, C.-T.; Liu, M.; Sargent, E. H.; Sinton, D. Nanomorphology-Enhanced Gas-Evolution Intensifies CO_2 Reduction Electrochemistry. *ACS Sustainable Chemistry & Engineering* **2017**, *5*, 4031–4040.

(66) van Brakel, J.; Heertjes, P. Analysis of diffusion in macroporous media in terms of a porosity, a tortuosity and a constrictivity factor. *International Journal of Heat and Mass Transfer* **1974**, *17*, 1093 – 1103.

(67) Hasted, J. B.; Ritson, D. M.; Collie, C. H. Dielectric Properties of Aqueous Ionic Solutions. Parts I and II. *The Journal of Chemical Physics* **1948**, *16*, 1–21.

(68) Bockris, J. O.; Reddy, A. K. *Volume 1: Modern Electrochemistry*, 2nd ed.; Springer US, 1998.

(69) Alnæs, M. S.; Blechta, J.; Hake, J.; Johansson, A.; Kehlet, B.; Logg, A.; Richardson, C.; Ring, J.; Rognes, M. E.; Wells, G. N. The FEniCS Project Version 1.5. *Archive of Numerical Software* **2015**, *3*, 9–23.

(70) Logg, A.; Mardal, K.-A.; Wells, G. N., et al. *Automated Solution of Differential Equations by the Finite Element Method*; Springer, 2012.

(71) Nitopi, S.; Bertheussen, E.; Scott, S. B.; Liu, X.; Engstfeld, A. K.; Horch, S.; Seger, B.; Stephens, I. E. L.; Chan, K.; Hahn, C.; NÃžrskov, J. K.; Jaramillo, T. F.; Chorkendorff, I. Progress and Perspectives of Electrochemical CO_2 Reduction on Copper in Aqueous Electrolyte. *Chemical Reviews* **2019**, *119*, 7610–7672.

(72) Kas, R.; Yang, K.; Bohra, D.; Kortlever, R.; Burdyny, T.; Smith, W. A. Electrochemical CO_2 reduction on nanostructured metal electrodes: fact or defect? *Chem. Sci.* **2020**, *11*, 1738–1749.

(73) Clark, E. L.; Resasco, J.; Landers, A.; Lin, J.; Chung, L.-T.; Walton, A.; Hahn, C.; Jaramillo, T. F.; Bell, A. T. Standards and Protocols for Data Acquisition and Reporting for Studies of the Electrochemical Reduction of Carbon Dioxide. *ACS Catalysis* **2018**, *8*, 6560–6570.

(74) Lee, C.; Zhao, B.; Lee, J. K.; Fahy, K. F.; Krause, K.; Bazylak, A. Bubble Formation in the Electrolyte Triggers Voltage Instability in CO_2 Electrolyzers. *iScience* **2020**, 101094.

(75) Liu, K.; Smith, W. A.; Burdyny, T. Introductory guide to assembling and operating gas diffusion electrodes for electrochemical CO_2 reduction. *ACS energy letters* **2019**, *4*, 639–643.

(76) Hou, C.-H.; Taboada-Serrano, P.; Yiacoumi, S.; Tsouris, C. Monte Carlo simulation of electrical double-layer formation from mixtures of electrolytes inside nanopores. *The Journal of Chemical Physics* **2008**, *128*, 044705.

(77) Cui, S. T.; Cochran, H. D. Molecular dynamics simulation of interfacial electrolyte behaviors in nanoscale cylindrical pores. *The Journal of Chemical Physics* **2002**, *117*, 5850–5854.

(78) Lian, C.; Jiang, D.-e.; Liu, H.; Wu, J. A Generic Model for Electric Double Layers in Porous Electrodes. *The Journal of Physical Chemistry C* **2016**, *120*, 8704–8710.

(79) Bae, J. H.; Han, J.-H.; Chung, T. D. Electrochemistry at nanoporous interfaces: new opportunity for electrocatalysis. *Phys. Chem. Chem. Phys.* **2012**, *14*, 448–463.

(80) Feng, G.; Qiao, R.; Huang, J.; Sumpter, B. G.; Meunier, V. Ion Distribution in Electrified Micropores and Its Role in the Anomalous Enhancement of Capacitance. *ACS Nano* **2010**, *4*, 2382–2390.

(81) Joekar-Niasar, V.; Schreyer, ·. L.; Sedighi, ·. M.; Icardi, M.; Huyghe, J. Coupled Processes in Charged Porous Media: From Theory to Applications. *Transport in Porous Media* **2019**, *130*, 183–214.